MOEM

Modern Electronic Materials 2024; 10(4): 217–226
DOI 10.3897/j.moem.10.4.142174

Research Article

Charge carrier distribution in the region of charged domain walls in reduced lithium niobate

Aleksandr M. Kislyuk[1], Mikhail D. Malinkovich[1], Tatiana S. Ilina[1], Ilya V. Kubasov[1], Dmitry A. Kiselev[1], Andrei V. Turutin[1], Vladimir P. Ivanov[1], Alexander A. Temirov[1], Viktor V. Kuts[1], Evelina E. Maksumova[1]

1 National University of Science and Technology "MISIS", 4-1 Leninsky Ave., Moscow 119049, Russian Federation

Corresponding author: Aleksandr M. Kislyuk (akislyuk94@gmail.com)

Received 19 October 2024 ♦ **Accepted** 16 December 2024 ♦ **Published** 30 December 2024

Citation: Kislyuk AM, Malinkovich MD, Ilina TS, Kubasov IV, Kiselev DA, Turutin AV, Ivanov VP, Temirov AA, Kuts VV, Maksumova EE (2024) Charge carrier distribution in the region of charged domain walls in reduced lithium niobate. *Modern Electronic Materials* 10(4): 217–226. https://doi.org/10.3897/j.moem.10.4.142174

Abstract

Charged domain walls (CDWs) in ferroelectric materials are of interest from both fundamental and applied perspectives due to their unique electrophysical properties, which differ significantly from those of the bulk material. Until recently, research efforts primarily focused on studying these properties, while less attention was given to the finite-thickness regions of CDWs with heterogeneous electrical conductivity. This study proposes a model describing the charge carrier distribution within the conductive region of CDWs. The dependencies of charge carrier concentration and mobility on the distance from the CDW were determined. An analytical expression for current-voltage characteristics, measurable by conductive atomic force microscopy (c-AFM), was also proposed. The model has been experimentally validated using AFM methods.

In particular, the Debye screening length of the electric field of head-to-head (H–H) CDWs by free charge carriers in strongly reduced $LiNbO_3$ crystals was found to be 90±10 nm. Additionally, the values of mobility and concentration of polarons forming the conductive H–H CDW were determined. The bound polaron concentration in this region is estimated to be approximately 30 times greater than in the monodomain region, reaching $\approx 3.8 \cdot 10^{17}$ cm^{-3}.

Keywords

lithium niobate, bidomain crystal, charged domain wall, diffusion annealing, reduction annealing, conductive atomic force microscopy

1. Introduction

One of the distinctive features of ferroelectric domain walls is the presence of a strong localized electric field induced by bound uncompensated ionic charges. Disruptions in structural periodicity, along with a high density of bound ionic charges, lead to localized changes in the electrophysical properties of the material near the domain walls. These changes manifest as impurity accumulation at interdomain boundaries [1], increased electrical conductivity [2–4], additional resonances in dielectric and mechanical impedance spectra [5], the emergence of memristive properties [6], changes in the refractive index, and enhanced birefringence [7, 8], as well as anomalies in Raman spectra [9–12]. Domain walls of any type can induce mechanical stresses in the crystal structure,

as evidenced, for instance, by X-ray topography data obtained from periodically polarized and polydomain crystals [8, 13].

The degree of charge, and consequently the properties of a ferroelectric domain wall, are characterized by the angle α between the direction of the spontaneous polarization vector P_s and the plane of the wall. The charge density at the boundary is proportional to $\sin(\alpha)$ [3, 14–16]. The morphology of charged domain walls (CDWs) is determined by a combination of material properties, particularly its crystalline structure and electrophysical characteristics. The presence of ionic charge significantly affects the kinetics of ferroelectric domain structure switching [17, 18].

One of the most intriguing materials for studying the formation of CDWs is the ferroelectric lithium niobate ($LiNbO_3$, LN). It features a uniaxial domain structure in which the spontaneous polarization vectors of adjacent domains are always antiparallel. Its thermal and chemical stability, high Curie temperature (approximately 1140 °C), lead-free composition, and commercial availability of wafers in various diameters and crystallographic cuts with reproducible properties make LN an ideal model system for investigating CDW properties [19]. Depending on the relative orientation of the spontaneous polarization vectors P_s in adjacent domains, three types of domain walls are distinguished in LN: head-to-tail, head-to-head (H–H), and tail-to-tail.

With the appropriate selection of technological parameters, it is possible to form a single extended, isolated CDW located at the mid-plane of the crystal (commonly referred to as a bidomain crystal) [20]. Bidomain crystals hold promise for applications in precision actuators [21–24], low-frequency vibration sensors [25, 26], magnetic field sensors (as part of composite magnetoelectrics) [27–29], and energy harvesting devices [30–32].

In contrast to ferromagnets, domain walls in ferroelectrics are ultrathin boundaries, (typically on the sub-nanometer scale when viewed at the level of atomic planes [33, 34]), and are often considered two-dimensional defects. CDWs are generally thicker than neutral ones [33]. However, results from high-resolution transmission electron microscopy reveal that, at the nanoscale, even neutral domain walls in LN exhibit meanders and kinks, leading to the presence of localized charged regions of the head-to-head or tail-to-tail type, where bound charges accumulate. Nevertheless, in terms of structure, the averaged thickness of a neutral CDW in LN is approximately 174 pm, equivalent to several lattice parameters [34].

At the same time, the thickness of the conductive channel formed by the compensation of the CDW electric field by free charge carriers significantly exceeds the structural thickness of the CDW itself [35]. Atomic force microscopy (AFM) techniques enable the localized investigation of electrophysical properties and visualization of the conductive channels thicknesses in CDWs [18, 36–38]. The thickness of the conductive channel is a critically important parameter, as it defines the volume near the CDW, which has a local electrical conductivity distinct from that of the surrounding bulk [39].

Until recently, despite extensive theoretical and experimental studies of ferroelectric domain walls, researchers primarily focused on their electrophysical properties. Less attention has been paid to the conductive region of CDW, which has finite thickness and heterogeneous electrical conductivity. This work presents a model describing the distribution of charge carriers near CDWs. The dependencies of charge carrier concentration and mobility on the distance from the CDW plane are derived, and an analytical expression for I–V characteristics measured using conductive atomic force microscopy is proposed.

2. Modeling

To describe the charge carrier concentrations in the CDW region, we use Poisson's equation, which in three-dimensional form is expressed as:

$$\Delta\varphi = -\frac{\rho(x,y,z)}{\varepsilon\varepsilon_0}, \tag{1}$$

where φ is electric potential, $\rho(x,y,z)$ is charge carrier density, $\varepsilon\varepsilon_0$ is absolute dielectric permittivity.

In the case of considering the concentration perpendicular to the CDW in a one-dimensional scenario, the equation takes the form:

$$\frac{\partial^2\varphi}{\partial z^2} = -\frac{\rho(z)}{\varepsilon\varepsilon_0}, \tag{2}$$

where z is the distance from the CDW along the crystallographic Z-axis.

Free charge carriers can accumulate near the CDW, compensating its ionic charge. Thus, the conditions of charge neutrality in the sample are satisfied: the total concentration of accumulated charge carriers equals the charges of the domain wall. An H–H type CDW accumulates negative charge carriers. The charge carrier density $\rho(z)$ can then be expressed as:

$$\rho(z) = e\Delta n(z) = en_0\left(e^{\frac{e\varphi(z)}{kT}} - 1\right), \tag{3}$$

where $n_0 e^{e\varphi(z)/k}$ is the spatial distribution of concentration of charge carriers screening the CDW field.

The differential equation is solved:

$$\frac{\partial^2\varphi}{\partial z^2} = -\frac{en_0}{\varepsilon\varepsilon_0}\left(e^{\frac{e\varphi(z)}{kT}} - 1\right). \tag{4}$$

Using the boundary conditions at $z \to \infty, \varphi \to 0$, constant of integration $C = -kT/e$ after the first integration, we obtain:

$$\left(\frac{\partial\varphi}{\partial z}\right)^2 = -\frac{2en_0kT}{\varepsilon\varepsilon_0}\left(e^{\frac{e\varphi}{kT}} - \frac{e\varphi}{kT} - 1\right). \tag{5}$$

Since the H–H CDW has a large ionic charge, the condition $e\varphi/kT \gg 1$ holds, then:

$$\frac{\partial\varphi}{\partial z} = \pm\sqrt{\frac{2n_0kT}{\varepsilon\varepsilon_0}}e^{\frac{e\varphi}{2kT}}, \quad (6)$$

$$\int e^{-\frac{e\varphi}{2kT}}\partial\varphi = \pm\sqrt{\frac{2n_0kT}{\varepsilon\varepsilon_0}}\int\partial z. \quad (7)$$

After integrating, we obtain:

$$-e^{-\frac{e\varphi(z)}{2kT}} + C' = \pm\frac{z}{\sqrt{2}L_D}, \quad (8)$$

where

$$L_D = \sqrt{\frac{\varepsilon\varepsilon_0kT}{e^2n_0}}.$$

Given that at $x = 0$, the potential equals the potential at the CDW $\varphi = \varphi_s$, the integration constant is:

$$C' = e^{-\frac{e\varphi_s}{2kT}}, \quad (9)$$

the equation then takes the form:

$$-e^{-\frac{e\varphi(z)}{2kT}} + e^{-\frac{e\varphi_s}{2kT}} = \pm\frac{z}{\sqrt{2}L_D}. \quad (10)$$

Since $e^{-e\varphi(z)/2kT}$ is always greater than $e^{-e\varphi s/2kT}$, and the value of $z/(\sqrt{2}L_D)$ is always positive, the right-hand side must have a negative sign. Finally, we have:

$$-e^{-\frac{e\varphi(z)}{2kT}} + e^{-\frac{e\varphi_s}{2kT}} = \pm\frac{z}{\sqrt{2}L_D}. \quad (11)$$

The potential dependence on the distance from the CDW $\varphi(z)$ is determined as follows:

$$\frac{e\varphi(z)}{kT} = 2\ln\frac{1}{\frac{z}{\sqrt{2}L_D} + e^{-\frac{e\varphi_s}{2kT}}}. \quad (12)$$

At $z = 0$, the charge carrier concentration at the CDW equals $n_s = n_0e^{e\varphi s/kT}$ then

$$e^{-\frac{e\varphi_s}{2kT}} = \sqrt{\frac{n_0}{n_s}}.$$

After simplification, the equation takes the form:

$$\frac{e\varphi(z)}{kT} = \ln\left(\frac{1}{\frac{z}{\sqrt{2}L_D} + \sqrt{\frac{n_0}{n_s}}}\right)^2. \quad (13)$$

The charge carrier concentration screening the CDW can then be calculated using the formula:

$$n(z) = n_0e^{\frac{e\varphi(z)}{kT}} = n_0\left(\frac{1}{\frac{z}{\sqrt{2}L_D} + \sqrt{\frac{n_0}{n_s}}}\right)^2. \quad (14)$$

Thus, the relationship between the charge concentration and the distance from the CDW reduces to determining L_D, which defines the width of the high-conductivity region near the CDW. The maximum carrier concentration at the CDW, n_s is determined by the potential at the CDW. The width of the conductive region can be experimentally determined using c-AFM images.

From Ohm's law in its differential form, the current density consists of two components: drift and diffusion. Assuming the current is positive when directed from the AFM probe into the sample under a positive probe potential, the total current density can be expressed as:

$$j = j_{\text{drift}} - j_{\text{diff}}. \quad (15)$$

We estimate the ratio between the drift and diffusion components. The drift current density is $j_{\text{drift}} = en\mu E \approx en\mu U/L$, where U is the voltage applied to the probe, and L is the characteristic distance from the probe where the potential approaches zero. Since

$$j_{\text{diff}} = -eD\frac{\partial n}{\partial r} \approx kT\mu\frac{n-n_0}{L}, \text{ the ratio}$$

$$\frac{j_{\text{drift}}}{j_{\text{diff}}} = \frac{en\mu\frac{U}{L}}{kT\mu\frac{n-n_0}{L}} = \frac{U}{U_0}\frac{1}{\left(1-\frac{n_0}{n}\right)} \gg 1,$$

as $U_0 = kT/e = 0.026$ V at room temperature and the AFM probe is subjected to a voltage of several volts. Thus, in this case, it is possible to neglect the diffusion component of the current and the total current will be determined by the drift component:

$$j = j_{\text{drift}} = e\mu n(r)E(r), \quad (16)$$

where r is the distance from the probe. To obtain an analytical expression for the I–V characteristics of reduced LN samples, including near the CDW, we use Poisson's equation in spherical coordinates to describe the potential generated by the probe:

$$\Delta\varphi(r,\theta,\alpha) = -\frac{\rho(r)}{\varepsilon(\alpha,\theta)\varepsilon_0}, \quad (17)$$

where α and θ are spherical coordinates. Since solving this equation analytically is not feasible, we simplify by averaging over the coordinates α and θ to express ε as an effective permittivity ε_{ef}:

$$\varepsilon = \varepsilon_{\text{ef}} = \frac{\varepsilon_{11}^T + \varepsilon_{22}^T + \varepsilon_{33}^T}{3} = 66, \quad (18)$$

where $\varepsilon_{ij}{}^T$ is the static dielectric permittivity of LN; $\varepsilon_{11}{}^T = \varepsilon_{22}{}^T = 84$, $\varepsilon_{33}{}^T = 30$. Equation (17) then becomes:

$$\frac{1}{r^2}\frac{\partial}{\partial r}\left(r^2\frac{\partial\varphi}{\partial r}\right) = -\frac{\rho(r)}{\varepsilon_{ef}\varepsilon_0}. \quad (19)$$

The differential Ohm's law (16) can be rewritten in terms of the current I and the distance from the probe r:

$$j = \frac{I}{2\pi r^2} = e\mu n(r)E(r), \tag{20}$$

from this we obtain:

$$n(r) = \frac{I}{2\pi r^2 e\mu E(r)}, \tag{21}$$

and Eq. (19) takes the form:

$$\frac{1}{r^2}\frac{\partial}{\partial r}\left(r^2\frac{\partial\varphi}{\partial r}\right) = -\frac{I}{2\pi\varepsilon\varepsilon_0 r^2\mu E(r)}, \tag{22}$$

after simplifying for r^2 and differentiating, we obtain:

$$2r\frac{\partial\varphi}{\partial r} + r^2\frac{\partial^2\varphi}{\partial r^2} = -\frac{I}{2\pi\varepsilon\varepsilon_0\mu E(r)}. \tag{23}$$

Assuming $E(r) = -\partial\varphi/\partial r$, the expression becomes:

$$2rE^2 + r^2EE' = \frac{I}{2\pi\varepsilon\varepsilon_0\mu}. \tag{24}$$

Solving this equation, we find the electric field intensity at a distance r from the probe

$$E = \sqrt{\frac{I}{3r\pi\varepsilon\varepsilon_0\mu}}. \tag{25}$$

The potential φ is then:

$$\varphi(r) = -\int E\mathrm{d}r = -\sqrt{\frac{I}{3\pi\varepsilon\varepsilon_0\mu}}\int\frac{1}{\sqrt{r}}\mathrm{d}r =$$

$$= -2\sqrt{\frac{Ir}{3\pi\varepsilon\varepsilon_0\mu}} + C''. \tag{26}$$

Assuming that at a certain distance r_{max} the potential due to the probe approaches zero: $r \to r_{max}$, $\varphi \to 0$,

$$\varphi(r_{max}) = -2\sqrt{\frac{Ir_{max}}{3\pi\varepsilon\varepsilon_0\mu}} + C'' = 0, \tag{27}$$

from this, the integration constant C" is determined as:

$$C'' = 2\sqrt{\frac{Ir_{max}}{3\pi\varepsilon\varepsilon_0\mu}}. \tag{28}$$

Therefore, the potential difference between the AFM probe with a tip radius of r_0 and r_{max} (or the applied voltage V) can be expressed as follows:

$$\Delta\varphi(r) = V = 2\sqrt{\frac{Ir_{max}}{3\pi\varepsilon\varepsilon_0\mu}}\left(1 - \sqrt{\frac{r_0}{r_{max}}}\right). \tag{29}$$

Consequently, the current-voltage dependence takes the form:

$$I = \frac{3\pi\varepsilon\varepsilon_0\mu V^2}{4r_{max}}\left(1 - \sqrt{\frac{r_0}{r_{max}}}\right)^{-2},$$

$$I = \beta\mu(T)V^2, \tag{30}$$

where

$$\beta = \frac{3}{4}\pi\varepsilon\varepsilon_0\left[r_{max}\left(1 - \sqrt{\frac{r_0}{r_{max}}}\right)^2\right]^{-1},$$

$\varepsilon \approx 66$ (based on the expression (18)), $r_0 \approx 8$ nm (according to the Hertzian model [40] for elastic interaction between the probe and the LN surface), and $r_{max} \approx 1$ μm (derived from the model of the electric field distribution of the probe near the CDW [41]). It has been experimentally demonstrated that under high electric field intensity beneath the AFM probe, the conduction mechanism is governed by space-charge-limited current (SCLC) [42–44] within the pre-electrode region, i.e., the local area where charge neutrality is disrupted.

3. Experimental

Commercially available congruent composition LN crystals with a crystallographic z-cut, manufactured by The Roditi International Corporation Ltd, were used as samples for the study. Rectangular specimens with dimensions of 10×10×0.5 mm^3, were cut from the plates, and a bidomain ferroelectric structure of the H–H type was subsequently formed in these specimens using the diffusion annealing method in air [22, 45, 46].

For AFM studies thin cross-sections of the crystals were prepared, oriented such that the polar Z-axis lay within the plane of the sample, and the nonpolar X-axis was perpendicular to the surface, as described in [18, 47–49]. One of the X-oriented surfaces of each of the resulting samples was polished to optical quality. To enhance conductivity and recrystallize the surface after mechanical treatment, the samples underwent a reducing annealing process at 1030 °C for 60 minutes in a ULVAC VHC-P610 infrared furnace under a dry nitrogen atmosphere (purity grade 6.0, 99.9999%). During annealing at this temperature in a reducing atmosphere, significant chemical reduction of the crystals occurs: molecular oxygen and lithium oxide evaporate from the crystal. This process is accompanied by the formation of antisite defects of niobium atoms at lithium positions Nb_{Li} and the release of four electrons resulting from the breaking of the covalent bond between Nb and O ions. The free electrons localize on structural Nb and antisite Nb_{Li}, forming small-radius free polarons and small-radius bound polarons, respectively.

After the reducing annealing, a chromium electrode was deposited on the side opposite the polished surface using magnetron sputtering. The samples were mounted onto a metallic substrate on the side of the chromium electrode using conductive silver paste (Leitsilber 200). c-AFM measurements were performed using an Asylum Research MFP-3D Stand Alone microscope. High-resolution silicon cantilevers with platinum coating (NSG10/Pt) were utilized. During scanning, 512 points

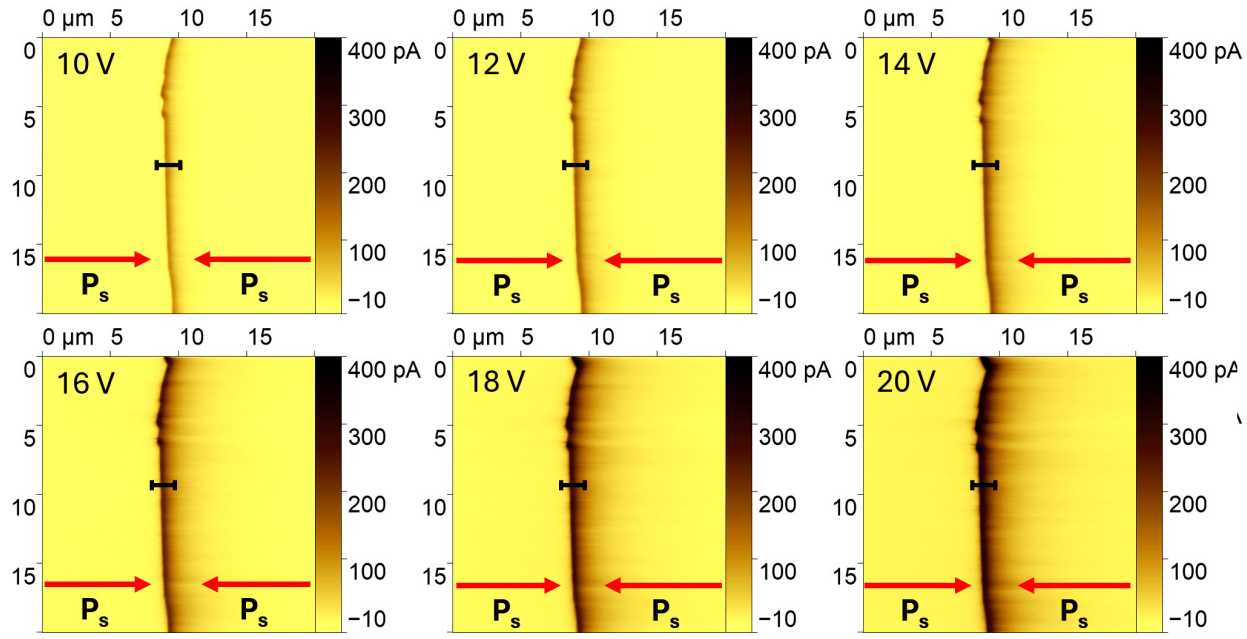

Figure 1. c-AFM images (trace mode) of the X-cut surface of a bidomain reduced LN crystal near H–H CDW (P_s denotes the direction of the spontaneous polarization vector), obtained at scanning voltages ranging from +10 V to +20 V

per line over a 20 μm area were recorded at a scanning frequency of 1 Hz.

4. Results and discussion

The value of L_D can be experimentally determined using c-AFM methods. It was observed that the width of the line having enhanced conductivity and associated with the CDW on current maps significantly increases with the intensity of the electric field applied by the probe. To determine the conductive width independently of the scanning voltage, current images of the CDW on the surface of reduced LN crystals were obtained at probe voltages ranging from 8 to 20 V, with a step of 2 V (Fig. 1). As expected, the H–H domain wall demonstrates significantly higher conductivity compared to the adjacent monodomain regions.

During scanning, images were recorded in both forward and reverse probe motion across the surface (trace and retrace mode). A current "drag" effect was observed in the direction of the probe's movement. On the current profiles across the CDW, this effect appears as a gradual decrease in current (Fig. 2). When the probe moves in the opposite direction, the drag occurs on the opposite side of the peak. This effect is presumably associated with the extraction of polarons from the CDW region due to the high electric field intensity of the probe.

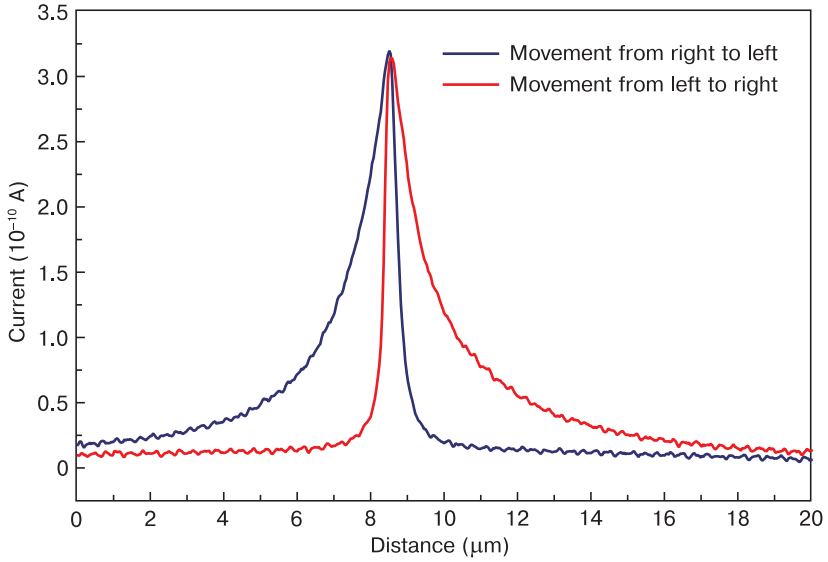

Figure 2. Current profiles of c-AFM images at a constant voltage of +20 V. The red line corresponds to the probe movement from left to right and the blue line corresponds to the movement from right to left

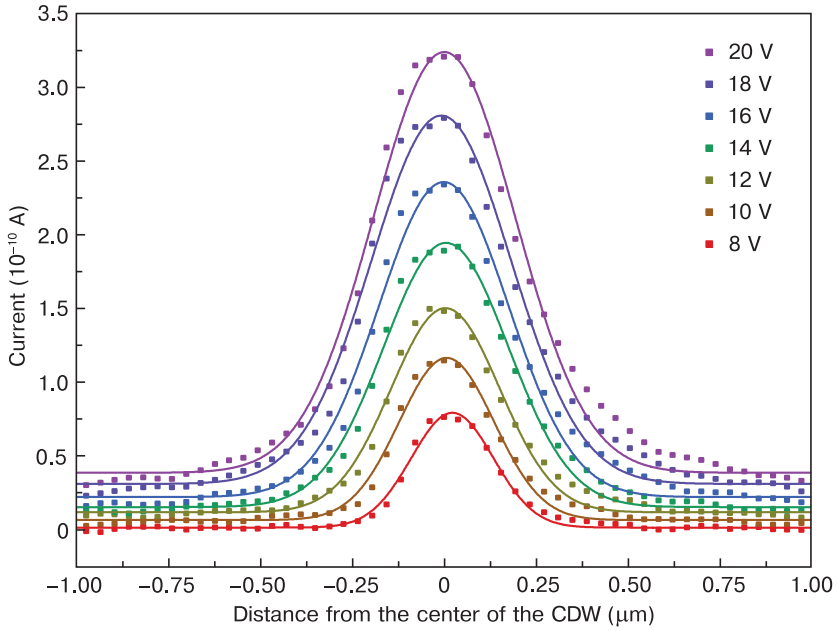

Figure 3. Current profiles, processed to minimize drag effects, obtained from the same region of the CDW at different scanning voltages (dots represent experimental data, while lines represent a Gaussian function fit)

The presence of current drag by the probe during scanning complicates the determination of the CDW field screening length. Since the current drag results from the probe's high-intensity field crossing the boundary, it becomes challenging to determine the Debye length of polarons in this region. However, current profiles recorded when approaching the CDW from different sides are nearly identical in amplitude and peak position. To address this, the sections of the profiles affected by current drag were removed, and the unaffected segments were combined into a unified cross-section. This approach enabled the construction of CDW current profiles for different scanning voltages with minimal influence of the current drag effect (Fig. 3). For each profile in Fig. 3, 10 lines from the same crystal area were averaged. The areas used for averaging these profiles are marked as section lines in Fig. 1.

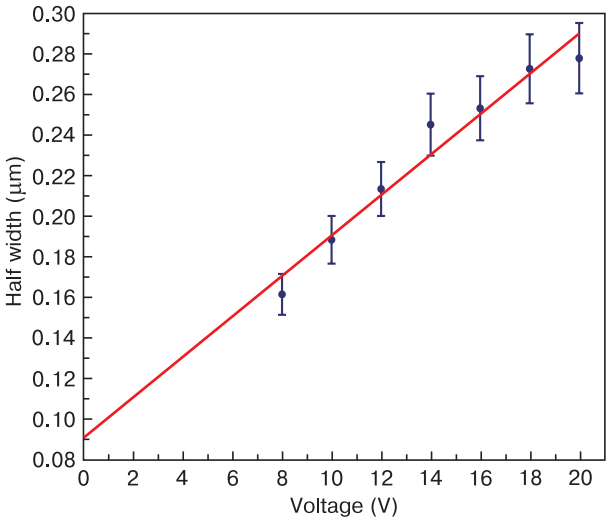

Figure 4. Dependence of half the width of the Gaussian function, measured at 1/*e* of its peak height and describing the current near the CDW, on the scanning voltage in the CDW screening region

The width of the current profiles increases with the scanning voltage. To determine the thickness of the conductive CDW channel (i.e., the width of the current profile independent of the scanning voltage), the obtained profiles were fitted with a Gaussian function. As the most accurate estimation of the Debye screening length, half the width of the Gaussian function at 1/*e* of the peak height was chosen. The resulting dependence was linearly extrapolated to 0 V, intersecting the ordinate axis at approximately 90±10 nm (Fig. 4).

Thus, the Debye screening length L_D of polarons is estimated. Given that

$$L_D = \sqrt{\frac{\varepsilon\varepsilon_0 kT}{e^2 n_0}},$$

the concentration of free carriers in the monodomain region is $n_0 \approx 1.1 \cdot 10^{16}$ cm^{-3}. The validity of the obtained value can be verified by determining the charge carrier concentration in reduced LN crystals using independent methods. The concentration of conducting polarons can be roughly estimated from the concentration of dissociated bipolarons at room temperature. This value is highly dependent on the reduction annealing conditions, thus representing an order-of-magnitude estimate. With a dissociation energy of 0.27 eV and under strong chemical reduction $n_0^{BP} = N_{\mathrm{Nb_{Li}}} \approx 9.2 \cdot 10^{20}$ cm^{-3} the dissociated bipolaron concentration is approximately $\approx 2.6 \cdot 10^{16}$ cm^{-3}. Concurrently, estimating the concentration from the conductivity ~10^{-9} Ω^{-1}·cm^{-1} [50–52] and

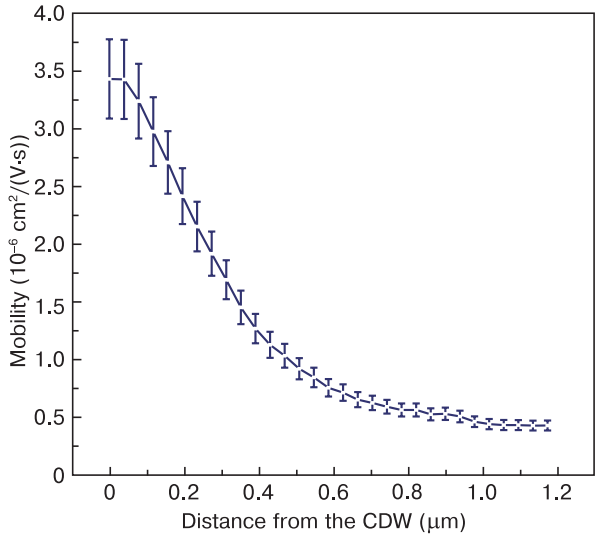

Figure 5. Charge carrier mobility as a function of distance from the CDW

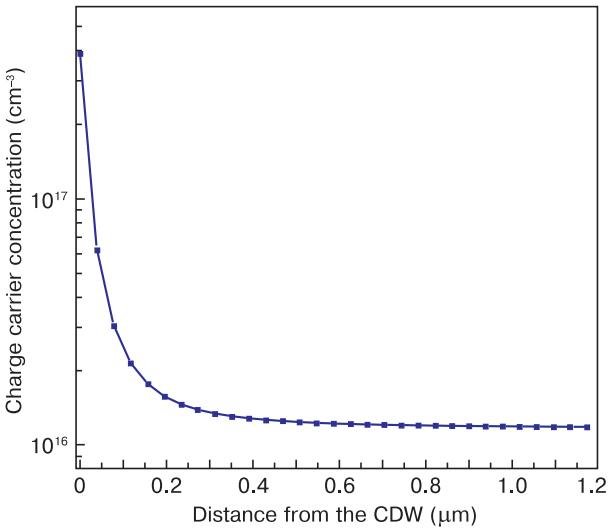

Figure 6. The dependence of charge carrier concentration on the distance from the CDW

mobility ~$5\cdot10^{-7}$ cm^2/(V·s) [18, 53] of the reduced crystals yields ~$1.25\cdot10^{16}$ cm^{-3}. These values are consistent with results calculated using the proposed model.

To determine the dependence of carrier concentration on distance from the CDW, the carrier concentration directly at the CDW (n_s) must be found. From thermodynamic equilibrium conditions for charge carriers screening the electric field, and using the Einstein relation, it is plausible to assume that the ratio of the charge carrier concentration far from the CDW (n_0) to the concentration at the CDW center n_0/n_s can be expressed as the ratio of their mobilities μ_0/μ_s. Using the proposed model, the mobility of charge carriers can be determined by linearizing the $I \sim V^2$ dependence. From the previously obtained current profiles, the linearized I–V^2 dependencies were extracted for each coordinate given in Fig. 3 in the CDW region. According to Eq. (30), knowing the slope and the coefficient β the mobility of carriers at a distance from the CDW can be expressed. This dependence is shown in Fig. 5. However, closer to the CDW, the linearization becomes less accurate, increasing the error in mobility determination. The obtained mobility values are consistent with the drift mobility of polarons reported in [53].

Using the ratio of mobilities far from the CDW to those at the CDW line, μ_0/μ_s, and Eqs (14) and (30), and the known value of n_0 the charge carrier concentration that screens the bound charges of the CDW is determined to be $n_s \approx 3.8\cdot10^{17}$ cm^{-3}. Using Eq. (14), the charge carrier concentration profile near the CDW can be estimated. The resulting concentration profile is shown in Fig. 6 and combines the charge carriers accumulated by the CDW and those present far from the CDW.

5. Conclusion

This work proposes a model describing the distribution of charge carriers in the conductive region near the CDW in reduced LN. According to the developed model, the CDW conductivity is inhomogeneous across the width of the conductive region. The distribution of free charge carriers is governed by the conditions of the sample's charge neutrality, which dictate that the total accumulated carrier concentration equals the charge of the domain wall. The Debye screening length of the electric field of the H–H type CDW by free carriers in reduced LN crystals is determined to be 90±10 nm. Accordingly, the total thickness of the CDW's conductive region is approximately 250 nm ($2\sqrt{2}L_D$), ignificantly exceeding its structural thickness.

Using the proposed model, the charge carrier concentrations screening the CDW field were calculated. For samples of reduced bidomain LN, the polaron concentration at the H–H type CDW exceeds that in the monodomain region by a factor of 30, reaching ≈$3.8\cdot10^{17}$ cm^{-3}. In reduced LN single crystals, the increased charge carrier concentration under the influence of the AFM probe's high electric field strength leads to the realization of space-charge-limited current (SCLC) conduction mechanisms.

Acknowledgments

The study was performed with financial support from the Russian Science Foundation (grant No. 24-29-20303, https://rscf.ru/en/project/24-29-20303/).

References

1. Aristov V.V., Kokhanchik L.S., Voronovskii Y.I. Voltage contrast of ferroelectric domains of lithium niobate in SEM. *Physica Status Solidi (a)*. 1984: 86(1): 133–141. https://doi.org/10.1002/pssa.2210860113
2. Seidel J., Fu D., Yang S.-Y., Alarcón-Lladó E., Wu J., Ramesh R., Ager J.W. Efficient photovoltaic current generation at ferroelectric domain walls. *Physical Review Letters*. 2011; 107(12): 126805. https://doi.org/10.1103/PhysRevLett.107.126805
3. Schröder M., Haußmann A., Thiessen A., Soergel E., Woike T., Eng L.M. Conducting domain walls in lithium niobate single crystals. *Advanced Functional Materials*. 2012; 22(18): 3936–3944. https://doi.org/10.1002/adfm.201201174
4. Schröder M., Chen X., Haußmann A., Thiessen A., Poppe J., Bonnell D.A., Eng L.M. Nanoscale and macroscopic electrical ac transport along conductive domain walls in lithium niobate single crystals. *Materials Research Express*. 2014; 1(3): 035012. https://doi.org/10.1088/2053-1591/1/3/035012
5. Nataf G.F., Aktas O., Granzow T., Salje E.K.H. Influence of defects and domain walls on dielectric and mechanical resonances in $LiNbO_3$. *Journal of Physics: Condensed Matter*. 2016; 28(1): 015901. https://doi.org/10.1088/0953-8984/28/1/015901
6. Chaudhary P., Lu H., Lipatov A., Ahmadi Z., McConville J.P.V., Sokolov A., Shield J.E., Sinitskii A., Gregg J.M., Gruverman A. Low-voltage domain-wall $LiNbO_3$ memristors. *Nano Letters*. 2020; 20(8): 5873–5878. https://doi.org/10.1021/acs.nanolett.0c01836
7. Kim S., Gopalan V. Optical index profile at an antiparallel ferroelectric domain wall in lithium niobate. *Materials Science and Engineering: B*. 2005; 120(1-3): 91–94. https://doi.org/10.1016/j.mseb.2005.02.029
8. Kim S., Gopalan V., Steiner B. Direct x-ray synchrotron imaging of strains at 180° domain walls in congruent $LiNbO_3$ and $LiTaO_3$ crystals. *Applied Physics Letters*. 2000; 77(13): 2051–2053. https://doi.org/10.1063/1.1312854
9. Stone G., Dierolf V. Influence of ferroelectric domain walls on the Raman scattering process in lithium tantalate and niobate. *Optics Letters*. 2012; 37(6): 1032. https://doi.org/10.1364/OL.37.001032
10. Taniguchi H., Fujii Y., Itoh M. Confocal micro-Raman imaging on 180°-domain structure in periodically poled stoichiometric $LiNbO_3$. *Journal of the Ceramic Society of Japan*. 2013; 121(1416): 579–582. https://doi.org/10.2109/jcersj2.121.579
11. Zelenovskiy P.S., Shur V.Y., Bourson P., Fontana M.D., Kuznetsov D.K., Mingaliev E.A. Raman study of neutral and charged domain walls in lithium niobate. Ferroelectrics. 2010; 398(1): 34–41. https://doi.org/10.1080/00150193.2010.489810
12. Rix J., Rüsing M., Galli R., Golde J., Reitzig S., Eng L.M., Koch E. Brillouin and Raman imaging of domain walls in periodically-poled 5%-MgO:$LiNbO_3$. *Optics Express*. 2022; 30(4): 5051. https://doi.org/10.1364/OE.447554
13. Irzhak D.V., Kokhanchik L.S., Punegov D.V., Roshchupkin D.V. Study of the specific features of lithium niobate crystals near the domain walls. *Physics of the Solid State*. 2009; 51(7): 1500–1502. https://doi.org/10.1134/s1063783409070452
14. Eliseev E.A., Morozovska A.N., Svechnikov G.S., Gopalan V., Shur V.Y. Static conductivity of charged domain walls in uniaxial ferroelectric semiconductors. *Physical Review B: Condensed Matter and Materials Physics*. 2011; 83(23): 235313. https://doi.org/10.1103/PhysRevB.83.235313
15. Wolba B., Seidel J., Cazorla C., Godau C., Haußmann A., Eng L.M. Resistor Network modeling of conductive domain walls in lithium niobate. *Advanced Electronic Materials*. 2018; 4(1): 1700242. https://doi.org/10.1002/aelm.201700242
16. Morozovska A.N. Domain wall conduction in ferroelectrics. *Ferroelectrics*. 2012; 438(1): 3–19. https://doi.org/10.1080/00150193.2012.744258
17. Kosobokov M., Turygin A., Melnikov S., Shur V., Alikin D. Role of domain wall conductivity in the stability of ferroelectric domains in ferroelectric single crystals. *Physical Review B*. 2024; 110(13): 134116. https://doi.org/10.1103/PhysRevB.110.134116
18. Kislyuk A.M., Ilina T.S., Kubasov I.V., Kiselev D.A., Temirov A.A., Turutin A.V., Malinkovich M.D., Polisan A.A., Parkhomenko Y.N. Tailoring of stable induced domains near a charged domain wall in lithium niobate by probe microscopy. *Modern Electronic Materials*. 2019; 5(2): 51–60. https://doi.org/10.3897/j.moem.5.2.51314
19. Kislyuk A.M., Kubasov I.V., Temirov A.A., Turutin A.V., Shportenko A.S., Kuts V.V., Malinkovich M.D. Electrophysical properties, memristive and resistive switching of charged domain walls in lithium niobate. *Modern Electronic Materials*. 2023; 9(4): 145–161. https://doi.org/10.3897/j.moem.9.4.116646
20. Kubasov I.V., Kislyuk A.M., Turutin A.V., Malinkovich M.D., Parkhomenko Y.N. Bidomain ferroelectric crystals: Properties and prospects of application. *Russian Microelectronics*. 2021; 50(8): 571–616. https://doi.org/10.1134/S1063739721080035
21. Kulikov A., Blagov A., Marchenkov N., Targonsky A., Eliovich Y., Pisarevsky Y., Kovalchuk M. $LiNbO_3$-based bimorph piezoactuator for fast X-ray experiments: Static and quasistatic modes. *Sensors and Actuators A: Physical*. 2019; 291(6): 68–74. https://doi.org/10.1016/j.sna.2019.03.041
22. Nakamura K., Shimizu H. Hysteresis-free piezoelectric actuators using $LiNbO_3$ plates with a ferroelectric inversion layer. *Ferroelectrics*. 1989; 93(1): 211–216. https://doi.org/10.1080/00150198908017348
23. Nakamura K. Antipolarity domains formed by heat treatment of ferroelectric crystals and their applications. *Japanese Journal of Applied Physics*. 1992; 31(S1): 9–13. https://doi.org/10.7567/JJAPS.31S1.9
24. Nakamura K., Nakamura T., Yamada K. Torsional actuators using $LiNbO_3$ plates with an inversion layer. *Japanese Journal of Applied Physics*. 1993; 32(5S): 2415–2417. https://doi.org/10.1143/JJAP.32.2415
25. Kubasov I.V., Kislyuk A.M., Turutin A.V., Bykov A.S., Kiselev D.A., Temirov A.A., Zhukov R.N., Sobolev N.A., Malinkovich M.D., Parkhomenko Y.N. Low-frequency vibration sensor with a sub-nm sensitivity using a bidomain lithium niobate crystal. *Sensors (Switzerland)*. 2019; 19(3): 614. https://doi.org/10.3390/s19030614
26. Kubasov I.V., Kislyuk A.M., Malinkovich M.D., Temirov A.A., Ksenich S.V., Kiselev D.A., Bykov A.S., Parkhomenko Y.N. A novel vibration sensor based on bidomain lithium niobate crystal. *Acta Physica Polonica A*. 2018; 134(1): 106–108. https://doi.org/10.12693/APhysPolA.134.106

27. Bichurin M.I., Petrov R.V., Leontiev V.S., Sokolov O.V., Turutin A.V., Kuts V.V., Kubasov I.V., Kislyuk A.M., Temirov A.A., Malinkovich M.D., Parkhomenko Y.N. Self-biased bidomain $LiNbO_3$/Ni/Metglas magnetoelectric current sensor. *Sensors*. 2020; 20(24): 7142. https://doi.org/10.3390/s20247142
28. Bichurin M.I., Sokolov O.V., Leontiev V.S., Petrov R.V., Tatarenko A.S., Semenov G.A., Ivanov S.N., Turutin A.V., Kubasov I.V., Kislyuk A.M., Malinkovich M.D., Parkhomenko Y.N., Kholkin A.L., Sobolev N.A. Magnetoelectric effect in the bidomain lithium niobate/nickel/metglas gradient structure. *Physica Status Solidi B*. 2020; 257(3): 1900398. https://doi.org/10.1002/pssb.201900398
29. Turutin A.V., Skryleva E.A., Kubasov I.V., Milovich F.O., Temirov A.A., Raketov K.V., Kislyuk A.M., Zhukov R.N., Senatulin B.R., Kuts V.V., Malinkovich M.D., Parkhomenko Y.N., Sobolev N.A. Magnetoelectric MEMS magnetic field sensor based on a laminated heterostructure of bidomain lithium niobate and metglas. *Materials*. 2023; 16(2): 484. https://doi.org/10.3390/ma16020484
30. Vidal J.V., Turutin A.V., Kubasov I.V., Kislyuk A.M., Malinkovich M.D., Parkhomenko Y.N., Kobeleva S.P., Pakhomov O.V., Sobolev N.A., Kholkin A.L. Low-frequency vibration energy harvesting with bidomain $LiNbO_3$ single crystals. *IEEE Transactions on Ultrasonics, Ferroelectrics, and Frequency Control*. 2019; 66(9): 1480–1487. https://doi.org/10.1109/TUFFC.2019.2908396
31. Vidal J.V., Turutin A.V., Kubasov I.V., Kislyuk A.M., Kiselev D.A., Malinkovich M.D., Parkhomenko Y.N., Kobeleva S.P., Sobolev N.A., Kholkin A.L. Dual vibration and magnetic energy harvesting with bidomain $LiNbO_3$-based composite. *IEEE Transactions on Ultrasonics, Ferroelectrics, and Frequency Control*. 2020; 67(6): 1219–1229. https://doi.org/10.1109/TUFFC.2020.2967842
32. Kubasov I.V., Kislyuk A.M., Malinkovich M.D., Temirov A.A., Ksenich S.V., Kiselev D.A., Bykov A.S., Parkhomenko Y.N. Vibrational power harvester based on lithium niobate bidomain plate. *Acta Physica Polonica A*. 2018; 134(1): 90–92. https://doi.org/10.12693/APhysPolA.134.90
33. Jia C.-L., Mi S.-B., Urban K., Vrejoiu I., Alexe M., Hesse D. Atomic-scale study of electric dipoles near charged and uncharged domain walls in ferroelectric films. *Nature Materials*. 2008; 7(1): 57–61. https://doi.org/10.1038/nmat2080
34. Gonnissen J., Batuk D., Nataf G.F., Jones L., Abakumov A.M., Van Aert S., Schryvers D., Salje E.K.H. Direct observation of ferroelectric domain walls in $LiNbO_3$: wall-meanders, kinks, and local electric charges. *Advanced Functional Materials*. 2016; 26(42): 7599–7604. https://doi.org/10.1002/adfm.201603489
35. Volk T.R., Gainutdinov R.V., Zhang H.H. Domain-wall conduction in AFM-written domain patterns in ion-sliced $LiNbO_3$ films. *Applied Physics Letters*. 2017; 110(13): 1–6. https://doi.org/10.1063/1.4978857
36. Alikin D.O., Ievlev A.V., Turygin A.P., Lobov A.I., Kalinin S.V., Shur V.Y. Tip-induced domain growth on the non-polar cuts of lithium niobate single-crystals. *Applied Physics Letters*. 2015; 106(18): 182902. https://doi.org/10.1063/1.4919872
37. Schultheiß J., Rojac T., Meier D. Unveiling alternating current electronic properties at ferroelectric domain walls. *Advanced Electronic Materials*. 2022; 8(6): 2100996. https://doi.org/10.1002/aelm.202100996
38. Guyonnet J., Gaponenko I., Gariglio S., Paruch P. Conduction at domain walls in insulating $Pb(Zr_{0.2}Ti_{0.8})O_3$ thin films. *Advanced Materials*. 2011; 23(45): 5377–5382. https://doi.org/10.1002/adma.201102254
39. Werner C.S., Herr S.J., Buse K., Sturman B., Soergel E., Razzaghi C., Breunig I. Large and accessible conductivity of charged domain walls in lithium niobate. *Scientific Reports*. 2017; 7(1): 9862. https://doi.org/10.1038/s41598-017-09703-2
40. Yablon D.G. (Ed.) Scanning probe microscopy in industrial applications. Hoboken (NJ): John Wiley & Sons, Inc.; 2013. https://doi.org/10.1002/9781118723111
41. Starkov A., Starkov I. Theoretical model of SPM-tip electrostatic field accounting for dead layer and domain wall. In: *Proceedings of ISAF-ECAPD-PFM 2012. 9-13 July 2012. Aveiro (Portugal)*. IEEE; 2012: 1–4. https://doi.org/10.1109/ISAF.2012.6297837
42. Gaffar M.A., Abousehly A.M., El-Fadl A.A., Mostafa M.M. Bulk- and electrode-limited conduction mechanisms in different phases of Mn^{2+}-doped potassium tetrachlorozincate crystal. *Journal of Physics D: Applied Physics*. 2005; 38(4): 577–583. https://doi.org/10.1088/0022-3727/38/4/009
43. Lian J., Tao J., Chai X., Zhang Y., Jiang A. Effects of atmosphere, metal films, temperatures and holding time on the surface topography and electrical conductivity of $LiNbO_3$ single crystals. *Ceramics International*. 2019; 45(8): 9736–9753. https://doi.org/10.1016/j.ceramint.2019.02.008
44. Kubasov I.V., Kislyuk A.M., Ilina T.S., Shportenko A.S., Kiselev D.A., Turutin A.V., Temirov A.A., Malinkovich M.D., Parkhomenko Y.N. Conductivity and memristive behavior of completely charged domain walls in reduced bidomain lithium niobate. *Journal of Materials Chemistry C*. 2021; 9(43): 15591–15607. https://doi.org/10.1039/d1tc04170c
45. Ohnishi N. An etching study on a heat-induced layer at the positive-domain surface of $LiNbO_3$. *Japanese Journal of Applied Physics*. 1977. 16(6): 1069–1070. https://doi.org/10.1143/JJAP.16.1069
46. Nakamura K., Ando H., Shimizu H. Partial domain inversion in $LiNbO_3$ plates and its applications to piezoelectric devices. In: *IEEE 1986 Ultrasonics Symposium, 17–19 November 1986. Williamsburg (VA, USA)*. IEEE; 1986: 719–722. https://doi.org/10.1109/ULTSYM.1986.198828
47. Kubasov I.V., Timshina M.S., Kiselev D.A., Malinkovich M.D., Bykov A.S., Parkhomenko Y.N. Interdomain region in single-crystal lithium niobate bimorph actuators produced by light annealing. *Crystallography Reports*. 2015; 60(5): 700–705. https://doi.org/10.1134/S1063774515040136
48. Shportenko A.S., Kislyuk A.M., Turutin A.V., Kubasov I.V., Malinkovich M.D., Parkhomenko Y.N. Effect of contact phenomena on the electrical conductivity of reduced lithium niobate. *Modern Electronic Materials*. 2021; 7(4): 167–175. https://doi.org/10.3897/j.moem.7.4.78569
49. Kislyuk A.M., Ilina T.S., Kubasov I.V., Kiselev D.A., Temirov A.A., Turutin A.V., Shportenko A.S., Malinkovich M.D., Parkhomenko Y.N. Degradation of the electrical conductivity of charged domain walls in reduced lithium niobate crystals. *Modern Electronic Materials*. 2022; 8(1): 15–22. https://doi.org/10.3897/j.moem.8.1.85251
50. Bordui P.F., Jundt D.H., Standifer E.M., Norwood R.G., Sawin R.L., Galipeau J.D., Norwood R.G., Jundt D.H., Bordui P.F., Standifer E.M., Sawin R.L., Jundt D.H., Standifer E.M., Norwood R.G., Sawin R.L., Galipeau J.D. Chemically reduced lithium niobate single crystals: Processing, properties and improved surface acoustic

wave device fabrication and performance. *Journal of Applied Physics*. 1999; 85(7): 3766–3769. https://doi.org/10.1063/1.369775

51. Dhar A., Singh N., Singh R.K., Singh R. Low temperature dc electrical conduction in reduced lithium niobate single crystals. *Journal of Physics and Chemistry of Solids*. 2013; 74(1): 146–151. https://doi.org/10.1016/j.jpcs.2012.08.011

52. Josch W., Munser R., Ruppel W., Wurfel P. The photovoltaic effect and the charge transport in $LiNbO_3$. *Ferroelectrics*. 1978; 21(1): 623–625. https://doi.org/10.1080/00150197808237347

53. Nagels P. Experimental Hall effect data for a small-polaron semiconductor. In: *The Hall Effect and Its Applications*. Boston (MA): Springer; 1980. P. 253–280. https://doi.org/10.1007/978-1-4757-1367-1